Fermi Surface Spin Texture and Topological Superconductivity in Spin-Orbit Free Noncollinear Antiferromagnets

Seung Hun Lee, Yuting Qian, and Bohm-Jung Yang*
Department of Physics and Astronomy, Seoul National University, Seoul 08826, Korea; Center for Theoretical Physics (CTP), Seoul National University, Seoul 08826, Korea; and Institute of Applied Physics, Seoul National University, Seoul 08826, Korea

(Received 29 August 2023; accepted 15 April 2024; published 10 May 2024)

We explore the relationship among the magnetic ordering in real space, the resulting spin texture on the Fermi surface, and the related superconducting gap structure in noncollinear antiferromagnetic metals without spin-orbit coupling. Via a perturbative approach, we show that noncollinear magnetic ordering in a metal can generate momentum-dependent spin texture on its Fermi surface, even in the absence of spin-orbit coupling, if the metal has more than three sublattices in its magnetic unit cell. Thus, our theory naturally extends the idea of altermagnetism to noncollinear spin structures. When superconductivity is developed in a magnetic metal, as the gap-opening condition is strongly constrained by the spin texture, the nodal structure of the superconducting state is also enforced by the magnetism-induced spin texture. Taking the noncollinear antiferromagnet on the kagome lattice as a representative example, we demonstrate how the Fermi surface spin texture induced by noncollinear antiferromagnetism naturally leads to odd-parity spin-triplet superconductivity with nontrivial topological properties.

DOI: 10.1103/PhysRevLett.132.196602

Introduction.—The pairing symmetry of superconductivity is governed by the symmetry which constrains the relative spin directions of electron pairs at opposite momenta on the Fermi surface (FS) [1]. Time-reversal T and inversion P symmetries are the representative examples, both of which guarantee the presence of energetically degenerate electrons at opposite momenta while they constrain the spin directions of the electron pairs in an opposite way. When both T and P exist simultaneously, spin-singlet superconductivity which can open a full gap on the spin-degenerate FS is mostly favored, unless the Cooper pairing with higher angular momentum is naturally favored due to the spatial modulation of repulsive interaction [2] or the pairing glue allows only spin-triplet channels [3,4]. Thus, to achieve unconventional pairing symmetries, such as spin-triplet superconductivity (STS), breaking either T or P is normally considered.

For instance, various unconventional superconducting states are proposed in T-symmetric metals with broken P symmetry [5–10]. In such noncentrosymmetric metals, as parity-mixing occurs due to P breaking, superconducting states can contain spin-triplet components. Moreover, when spin-orbit coupling (SOC) is present, the T-symmetric spin-split FS can host a spin-momentum locked winding spin texture, which leads to STS with intriguing nodal structure [6]. Because of the Kramers' degeneracy at T-invariant momenta, such winding spin texture carries a topological charge and appears robustly [11]. However, unless the superconducting state is dominated by spin-triplet components, observing nodal STS is not easy to achieve.

On the other hand, in centrosymmetric magnetic metals preserving P but breaking T, equal-spin triplet pairing can naturally arise because P enforces electron pairs at opposite momenta to have the same spin direction. Thus, if the FS is spin split, P-symmetric magnetic metals are promising candidates to achieve STS. Interestingly, as shown in Ref. [12], such a spin-split FS with fixed spin polarization can appear not only in ferromagnets but also in collinear antiferromagnets when P is broken locally but preserved globally [12–15]. Thus, centrosymmetric collinear magnetic metals can also host odd-parity STS. However, in such systems, the FS generally does not have robust spin texture even when SOC exists. This is because, as the Kramers' degeneracy is lifted due to broken T, winding spin texture with topological stability does not appear in general [11,16]. Therefore, to achieve nodal STS in centrosymmetric magnets, a distinct mechanism to protect winding spin texture is necessary.

In this Letter, we study how real space magnetic ordering of a centrosymmetric non-collinear antiferromagnetic (AFM) metal induces winding spin texture on the FS without SOC, which in turn constrains the gap structure of its superconducting state. Through a perturbation approach, we show that if the number of sublattices in a magnetic unit cell is larger than two, the FS can have momentum-dependent, winding spin texture. Thus, our theory extends the idea of altermagnetism proposed recently [14,15,17–23] to the cases of noncollinear antiferromagnets without SOC. We demonstrate our theory in a kagome noncollinear

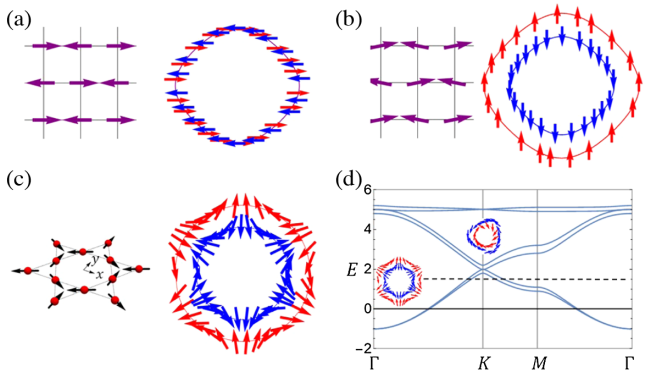

FIG. 1. (a) The FSST of a collinear antiferromagnet in the square lattice ($\boldsymbol{m}_1 = -\boldsymbol{m}_2$). The FS is spin degenerate while the spin direction is parallel to the AFM ordering direction. (b) The FSST of a canted antiferromagnet ($\boldsymbol{m}_1 + \boldsymbol{m}_2 \neq 0$). The FS is spin split while the spin direction on each FS is uniform. (c) The kagome AIAO AFM structure (left) and the corresponding FSST (right) computed when $m = 0.2$ and $\mu = -3.0$. (d) The energy eigenvalues of $\mathcal{H}_{\mathrm{KAFM}}(\boldsymbol{k})$ calculated along high-symmetry momentum directions. The FSST for $\mu = -3.0$ (-1.5) at which the FS encloses the Γ (K and K') is also plotted. The solid (dotted) black horizontal line indicates the Fermi level at $\mu = -3.0$ (-1.5).

antiferromagnet with three sublattices. As a result of magnetism-induced winding spin texture on the FS, we find various types of topological superconductors (TSCs) with the odd-parity spin-triplet pairing, including nodal TSCs, and first-order and second-order TSCs.

Magnetic ordering and FS spin texture.—To model a generic AFM metal with n sublattices in its magnetic unit cell, we construct a tight-binding Hamiltonian $\hat{H} = \sum_{\boldsymbol{k}} \hat{\boldsymbol{c}}_{\boldsymbol{k}}^{\dagger} \mathcal{H}(\boldsymbol{k}) \hat{\boldsymbol{c}}_{\boldsymbol{k}}$ where we take the basis $\hat{\boldsymbol{c}}_{\boldsymbol{k}}^{\dagger} = (\hat{c}_{\boldsymbol{k}1\uparrow}^{\dagger}, \hat{c}_{\boldsymbol{k}1\downarrow}^{\dagger}, \hat{c}_{\boldsymbol{k}2\uparrow}^{\dagger}, \hat{c}_{\boldsymbol{k}2\downarrow}^{\dagger}, \ldots, \hat{c}_{\boldsymbol{k}n\uparrow}^{\dagger}, \hat{c}_{\boldsymbol{k}n\downarrow}^{\dagger})$. When $n = 2$, we have

$$\mathcal{H}(\boldsymbol{k}) = \begin{pmatrix} h_{11}(\boldsymbol{k}) & h_{12}(\boldsymbol{k}) \\ h_{21}(\boldsymbol{k}) & h_{22}(\boldsymbol{k}) \end{pmatrix}, \tag{1}$$

where $h_{ij}(\boldsymbol{k})$ ($i, j = 1, 2$) are 2×2 block Hamiltonians. The diagonal blocks $h_{ii}(\boldsymbol{k}) = -\boldsymbol{m}_i \cdot \boldsymbol{\sigma}$ describe mean-field approximated local spin orders represented by a constant vector $\boldsymbol{m}_i$, while the off-diagonal blocks $h_{12}(\boldsymbol{k}) = h_{\mathrm{NN}}(\boldsymbol{k})\sigma_0 = h_{21}^{\dagger}(\boldsymbol{k})$ describe the kinetic part of the Hamiltonian coming from the nearest-neighbor (NN) hopping between different sublattices.

The Green's function of $\mathcal{H}(\boldsymbol{k})$ is given by $G(\boldsymbol{k}, \varepsilon) = [\varepsilon I_{4\times4} - \mathcal{H}(\boldsymbol{k})]^{-1}$, where ε is the energy and $I_{l\times l}$ is the identity matrix of dimension l [24]. From $g_{ii}(\boldsymbol{k}, \varepsilon)$, the 2×2 diagonal blocks of $G(\boldsymbol{k}, \varepsilon)$, we extract the effective Hamiltonian $h_{\mathrm{eff}}^{i}(\boldsymbol{k}, \varepsilon)$ projected onto the ith sublattice by using the equation $g_{ii}(\boldsymbol{k}, \varepsilon) = [\varepsilon I_{2\times2} - h_{\mathrm{eff}}^{i}(\boldsymbol{k}, \varepsilon)]^{-1}$. For instance, we obtain

$$\begin{aligned} h_{\mathrm{eff}}^{1}(\boldsymbol{k}, \varepsilon) &= h_{11}(\boldsymbol{k}) + h_{12}(\boldsymbol{k})[\varepsilon I_{2\times2} - h_{22}(\boldsymbol{k})]^{-1} h_{21}(\boldsymbol{k}) \\ &= -\boldsymbol{m}_1 \cdot \boldsymbol{\sigma} + |h_{\mathrm{NN}}(\boldsymbol{k})|^2 [\varepsilon I_{2\times2} + \boldsymbol{m}_2 \cdot \boldsymbol{\sigma}]^{-1} \\ &= -\boldsymbol{m}_1 \cdot \boldsymbol{\sigma} + \frac{|h_{\mathrm{NN}}(\boldsymbol{k})|^2}{m_2^2 - \varepsilon^2} [\varepsilon I_{2\times2} - \boldsymbol{m}_2 \cdot \boldsymbol{\sigma}] \end{aligned} \tag{2}$$

for $i = 1$.

If we separate the effective Hamiltonian into spin-independent and spin-dependent parts as $h_{\mathrm{eff}}^{1}(\boldsymbol{k}, \varepsilon) = R_0^1(\boldsymbol{k}, \varepsilon)\sigma_0 + \boldsymbol{R}^1(\boldsymbol{k}, \varepsilon) \cdot \boldsymbol{\sigma}$, Eq. (2) gives $\boldsymbol{R}^1(\boldsymbol{k}, \varepsilon) = -[\boldsymbol{m}_1 + \boldsymbol{m}_2 |h_{\mathrm{NN}}(\boldsymbol{k})|^2 / (m_2^2 - \varepsilon^2)]$. Since the FS is an equienergy contour, $|h_{\mathrm{NN}}(\boldsymbol{k})|^2$ and ε are constant on the FS. Hence $\hat{R}^1(\boldsymbol{k}, \varepsilon) \equiv \boldsymbol{R}^1(\boldsymbol{k}, \varepsilon)/|\boldsymbol{R}^1(\boldsymbol{k}, \varepsilon)|$ is uniform on the FS for a given Fermi level as shown in Figs. 1(a) and 1(b). One can see that when $\boldsymbol{m}_2 \nparallel \boldsymbol{m}_1$, the correction term from $h_{22}(\boldsymbol{k})$ in Eq. (2), proportional to $\boldsymbol{m}_2 \cdot \boldsymbol{\sigma}$, tilts $\hat{R}^1(\boldsymbol{k}, \varepsilon)$ away from (towards) $\boldsymbol{m}_1$ ($\boldsymbol{m}_2$).

In the presence of additional terms such as the next-nearest-neighbor (NNN) hopping that enters $h_{11}(\boldsymbol{k})$ and $h_{22}(\boldsymbol{k})$ in the form of $h_{\mathrm{NNN}}(\boldsymbol{k})\sigma_0$, the direction of $\boldsymbol{R}^1(\boldsymbol{k}, \varepsilon)$ may depend on $\boldsymbol{k}$. Nevertheless, $\boldsymbol{m}_1$ and $\boldsymbol{m}_2$ cannot generate smooth "winding" FS spin texture (FSST) when $n = 2$. This is because, to achieve winding FSST, there should be a momentum $\boldsymbol{k}'$ that satisfies $\hat{R}^1(\boldsymbol{k}', \varepsilon) = -\hat{R}^1(\boldsymbol{k}, \varepsilon)$ for an arbitrary $\boldsymbol{k}$. However, this condition can never be fulfilled unless $\boldsymbol{m}_1$ and $\boldsymbol{m}_2$ are either parallel or antiparallel. If they are parallel or antiparallel, Eq. (2) gives $\hat{R}^1(\boldsymbol{k}', \varepsilon) \| \boldsymbol{m}_1 \| \boldsymbol{m}_2$. The recently proposed altermagnets belong to this case [14,15].

On the other hand, when $n \geq 3$, the FS spin direction can be momentum dependent in general. For $n = 3$, we obtain $\boldsymbol{R}^1(\boldsymbol{k}, \varepsilon) = -\boldsymbol{m}_1 - \mathfrak{f}(\boldsymbol{k})\boldsymbol{m}_2 - \mathfrak{g}(\boldsymbol{k})\boldsymbol{m}_3 - \mathfrak{h}(\boldsymbol{k})(\boldsymbol{m}_2 \times \boldsymbol{m}_3)$, where $\mathfrak{f}(\boldsymbol{k})$, $\mathfrak{g}(\boldsymbol{k})$ and $\mathfrak{h}(\boldsymbol{k})$ are $\boldsymbol{k}$-dependent functions whose explicit forms are provided in Supplemental Material [25]. Since $\boldsymbol{R}^i(\boldsymbol{k})$ for a given ε is a real vector field in the momentum space, it can have a winding number w on the FS if (i) $\boldsymbol{R}^i(\boldsymbol{k})$ is confined in a two-dimensional plane and (ii) the FS is a closed curve enclosing singular points $\boldsymbol{k}_{c=1,2,\ldots,n_c}$ where $\boldsymbol{R}^i(\boldsymbol{k}_c, \varepsilon) = 0$. Then, $w = \sum_{c=1}^{n_c} v_c$ where v_c is the vorticity of the cth singular point. This condition can be satisfied with an appropriate choice of $h_{ij}(\boldsymbol{k})$ terms. Notably, the presence of the $\mathfrak{h}(\boldsymbol{k})$ term, which originates from the higher-order correction term, proportional to $(\boldsymbol{m}_2 \cdot \boldsymbol{\sigma})(\boldsymbol{m}_3 \cdot \boldsymbol{\sigma})$, indicates that the dimension of $\boldsymbol{R}^i(\boldsymbol{k})$ can be higher than what $\boldsymbol{m}_{i=1,2,3}$ can span in general [46]. However, if it is possible to choose the real gauge for the kinetic part of the Hamiltonian owing to symmetries such as $C_{2z}T$ in two-dimensions (2D) where $C_{m\alpha}$ is the m-fold rotation about the α axis or PT in two- or three-dimensions (3D), $\mathfrak{h}(\boldsymbol{k})$ vanishes for a generic $\boldsymbol{k}$ [25,47,48]. Because of this, especially in 2D, the winding number of FSST is well defined only when (i) $C_{2z}T$ or PT is present [so $\mathfrak{h}(\boldsymbol{k}) = 0$] and (ii) $\boldsymbol{m}_{i=1,2,3}$ are linearly dependent, or, equivalently, $\boldsymbol{m}_{i=1,2,3}$ are coplanar but not parallel to each

other. The kagome noncollinear antiferromagnet is an example that satisfies the above conditions.

Kagome noncollinear antiferromagnet.—As an example demonstrating the relation among the FSST, real space magnetic ordering, and pairing symmetries [10,12,49,50], we consider the kagome lattice noncollinear antiferromagnet whose structure is intrinsically P symmetric globally but P asymmetric locally.

The ground state of the classical Heisenberg AFM with Dzyaloshinskii-Moriya interaction on the kagome lattice is known to have coplanar 120° ordering lying in the lattice plane, in which the angles between NN spins are all 120° [51]. Among the infinitely degenerate coplanar 120° ordered states, we choose the so-called all-in-all-out (AIAO) order [Fig. 1(c)] that has three in-plane twofold rotation symmetries which are the elements of the D_{3d} point group.

We construct a tight-binding Hamiltonian $\mathcal{H}_{\mathrm{KAFM}}(\boldsymbol{k})$ describing the kagome AIAO antiferromagnet as in Eq. (1) but with $n = 3$. Explicitly, we have $h_{12} = -t(1 + e^{i\boldsymbol{k}\cdot\boldsymbol{e}_1})$, $h_{13} = -t(1 + e^{-i\boldsymbol{k}\cdot\boldsymbol{e}_3})$, $h_{23} = -t(1 + e^{i\boldsymbol{k}\cdot\boldsymbol{e}_2})$, and $h_{ii}(\boldsymbol{k}) = -\mu - \boldsymbol{m}_i \cdot \boldsymbol{\sigma}$ where $\boldsymbol{e}_1 = (1, 0)$, $\boldsymbol{e}_2 = (-1/2, \sqrt{3}/2)$, $\boldsymbol{e}_3 = (-1/2, -\sqrt{3}/2)$, $\boldsymbol{m}_1 = m(-\sqrt{3}/2, -1/2)$, $\boldsymbol{m}_2 = m(\sqrt{3}/2, -1/2)$, and $\boldsymbol{m}_3 = m(0, 1)$. Here, $t = 1$, m, and μ indicate the NN hopping amplitude, local magnetic moment, and chemical potential, respectively. In Fig. 1(d), we show the corresponding band structure for $m = 0.2$ and $\mu = -3.0$. The $\boldsymbol{R}^i$ field of the kagome AIAO antiferromagnet has singular points with total vorticity -2 $(+1)$ near the Γ point (K and K' points). Therefore, the two Fermi pockets that enclose Γ carry $w = -2$ FSST as in Fig. 1(c), while the pockets that enclose K or K' carry $w = 1$. The relevant FSSTs are also shown in Fig. 1(d). This example clearly demonstrates that FSST can be generated by real space magnetic ordering in the absence of SOC [52–54].

In addition, the vanishing $\boldsymbol{R}^i$ field at the singular points implies possible twofold degeneracies of spin bands. In Fig. 1(d), among the nodes at C_{3z}-invariant momenta protected by C_{3z} and $C_{2z}T$ symmetries, the gap closings between the first and second lowest bands at Γ and the fifth and sixth lowest bands at K (K') are such nodes. We note that the band touching between the second and third lowest bands at K (K') shows quadratic dispersion, even though the FSST winds only once. This happens because the physical spin (winding once) is different from the pseudospin (winding twice) defined in the projected two-band space related to the band crossing.

FSST and superconducting gap structure.—The spin structure of spin-triplet Cooper pairs can be described by the so-called d vector [1]. Thus, the effect of the FSST on Cooper pairs can be understood from the relation between the d vector and the FS spin direction. With Pauli matrices $\sigma_{x,y,z}$ that act on spin degrees of freedom, the mean-field pairing interaction can be written in a simple form

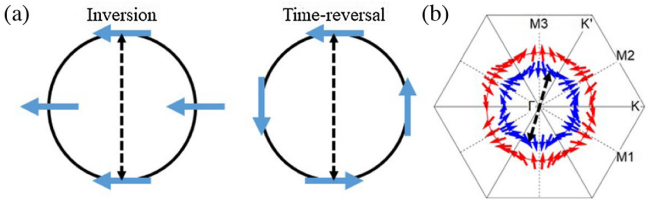

FIG. 2. (a) Schematic diagram describing the FS spin direction with P (left) and T (right) symmetries. (b) The FSST of $\mathcal{H}_{\mathrm{eff}}$ that corresponds to Fig. 1(c). The in-plane twofold rotation axes and the mirror invariant lines are represented by dashed and solid lines, respectively. The black dashed arrow connects the electron pair at opposite momenta for each case.

$\hat{H}_{\mathrm{int}} = \sum_{\boldsymbol{k},s,s'} \Delta_{\boldsymbol{k}} \hat{c}^{\dagger}_{\boldsymbol{k},s} \hat{c}^{\dagger}_{-\boldsymbol{k},s'} + \mathrm{H.c.}$, where $\Delta_{\boldsymbol{k}} = \psi_0(\boldsymbol{k})(i\sigma_y) + \boldsymbol{d}(\boldsymbol{k}) \cdot \boldsymbol{\sigma}(i\sigma_y)$ and s (s') denotes the spin. For a given spin basis, the d_z component indicates opposite-spin triplet pairing, while the d_x and d_y components describe equal-spin triplet pairing. As shown in Fig. 2(a), if P is present while T is absent, the equal-spin Cooper pairing is forced in the weak-coupling limit, because electron pairs at opposite momenta have the same spins. Therefore, for the spin basis aligned to the FSST direction, $\boldsymbol{d}(\boldsymbol{k})$ should have a component perpendicular to the FSST to open a gap on the FS. On the other hand, if T is present while P is absent, the opposite-spin Cooper pairing is forced, so the pairing interaction should have a $\boldsymbol{d}(\boldsymbol{k})$ component that is parallel to the FSST to open a gap.

To describe the superconducting state of the kagome antiferromagnet, we introduce pairing interaction $\Delta(\boldsymbol{k})$ and rewrite the Hamiltonian in the Nambu basis $\hat{\Psi}^{\dagger}_{\boldsymbol{k}} = (\hat{\boldsymbol{c}}^{\dagger}_{\boldsymbol{k}}, \hat{\boldsymbol{c}}_{-\boldsymbol{k}})$. Then, the Bogoliubov–de Gennes (BdG) Hamiltonian becomes $\sum_{\boldsymbol{k}} \hat{\Psi}^{\dagger}_{\boldsymbol{k}} \mathcal{H}_{\mathrm{BdG}}(\boldsymbol{k}) \hat{\Psi}_{\boldsymbol{k}}$ with

$$\mathcal{H}_{\mathrm{BdG}}(\boldsymbol{k}) = \begin{pmatrix} \mathcal{H}_{\mathrm{KAFM}}(\boldsymbol{k}) - \mu & \Delta(\boldsymbol{k}) \\ \Delta^{\dagger}(\boldsymbol{k}) & -\mathcal{H}^{T}_{\mathrm{KAFM}}(-\boldsymbol{k}) + \mu \end{pmatrix}. \quad (3)$$

Since $\mathcal{H}_{\mathrm{KAFM}}(\boldsymbol{k})$ is symmetric under D_{3d} point group symmetries, the pairing channels can be classified by corresponding irreducible representations (IRs) [1]. As the AIAO AFM state is P symmetric but T broken, equal-spin triplet pairing is favored, and thus only odd-parity spin-triplet IRs (A_{1u}, A_{2u}, and E_u) can induce superconducting instability within the weak-coupling approximation. The transformation properties of the IRs under the D_{3d} point group are summarized in Supplemental Material [25].

To illustrate the relation between the gap structure and FSST, we consider the FS with $w = 2$ near Γ shown in Fig. 1(d) as an example. Projecting the Hamiltonian $\mathcal{H}$ onto the lowest energy band of the nonmagnetic kagome lattice Hamiltonian $\mathcal{H}_{\mathrm{KAFM}}(\boldsymbol{k})|_{\boldsymbol{m}_i=0}$ and expanding it up to the quadratic order of k_x and k_y, we obtain the effective Hamiltonian near Γ given by

$$\mathcal{H}_{\rm eff}(\boldsymbol{k}) = (-4 + k_x^2 + k_y^2) + \frac{m}{6} k_x k_y \tau_x + \frac{m}{12}(k_x^2 - k_y^2)\tau_y, \qquad (4)$$

where the Pauli matrices $\tau_{i=1,2,3}$ denote the effective spin that represents the lowest two bands in Fig. 1(d). For $\mathcal{H}_{\rm eff}(\boldsymbol{k})$, the matrix representations of the D_{3d} symmetry generators are given by $C_{3z} = (\tau_0 - i\sqrt{3}\tau_z)/2$, $C_{2y} = i\tau_y$, and $P = \tau_0$.

Let us first consider $\Delta_{\boldsymbol{k}}^{A_{1u}}$, the pairing interaction belonging to the A_{1u} IR. As it satisfies $C_{2y}(\boldsymbol{k})\Delta_{\boldsymbol{k}}^{A_{1u}}(\boldsymbol{k})C_{2y}^T(\boldsymbol{k}) = \Delta_{C_{2y}\boldsymbol{k}}^{A_{1u}}$, d_x and d_z components, which couple to $\tau_x(i\tau_y)$ and $\tau_z(i\tau_y)$ in $\Delta_{\boldsymbol{k}}^{A_{1u}}$, respectively, are forbidden on the k_y axis. As displayed in Fig. 2(b), the effective spin texture on the k_y axis is pointing to the y direction, parallel to the d vector of $\Delta_{\boldsymbol{k}}^{A_{1u}}$, thus $\Delta_{\boldsymbol{k}}^{A_{1u}}$ cannot open a gap on the k_y axis. Similar arguments can also be applied to two other in-plane twofold rotation axes. Thus, $\Delta_{\boldsymbol{k}}^{A_{1u}}$ cannot open a gap at the intersection of the FS and the $\Gamma - M_{i=1,2,3}$ lines.

On the other hand, $\Delta_{\boldsymbol{k}}^{A_{2u}}$ satisfies $M_y(\boldsymbol{k})\Delta_{\boldsymbol{k}}^{A_{2u}}(\boldsymbol{k})M_y^T(\boldsymbol{k}) = \Delta_{M_y\boldsymbol{k}}^{A_{2u}}$ where $M_y = PC_{2y}$ is a mirror reflection with respect to the zx plane. Thus, the d vector of $\Delta_{\boldsymbol{k}}^{A_{2u}}$ is parallel to the spin texture on the k_x axis, both aligned to the y direction. As a result, $\Delta_{\boldsymbol{k}}^{A_{2u}}$ has nodes along the mirror invariant lines ($\Gamma - K$, $\Gamma - K'$, and $K - K'$).

Finally, in the case of the E_u IR, there are no such constraints for the direction of the d vector (see Supplemental Material [25]).

Topological superconductivity.—Consistent with the gap structure analysis by comparing the d-vector direction and FSST, one can find that the superconducting state is always gapped for the E_u pairing. Meanwhile, for the A_{1u} or A_{2u} pairing, the bulk is gapless if the FS intersects high-symmetry lines where the d vector is parallel to the FSST, unless the FS avoids such high-symmetry lines. To reveal the nature of the superconducting states in the kagome antiferromagnet, we investigate the nodal and topological structures of the BdG Hamilitonian in Eq. (3) in weak-pairing limit by varying μ and m, as summarized in Fig. 3. We note that the A_{2u} pairing makes the system gapless with point nodes on the mirror-invariant lines in every region of the $m - \mu$ parameter space where the normal state is metallic. In contrast, while the A_{1u} pairing mostly induces gapless superconducting states with nodes along the C_2-invariant lines, it can also induce a fully gapped superconductor in the green-colored regions in Fig. 3(a) where the FS does not cross the C_2-invariant lines. In both the A_{1u} and A_{2u} pairings, as the nodes are located along high-symmetry lines, pair annihilation between neighboring nodes can sometimes happen when the pairing interaction is strong enough. The resulting gapped superconducting state can become a second-order TSC as shown in the red region in Fig. 3(a).

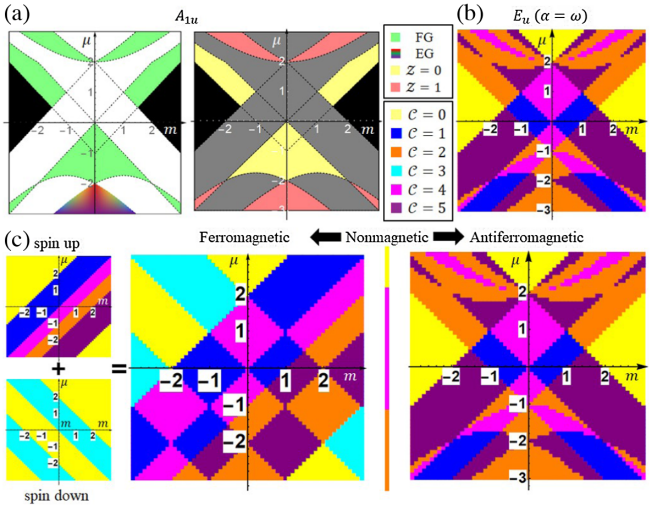

FIG. 3. (a) The topological phase diagrams for the A_{1u} IR obtained in the weak pairing limit. In the black-colored region, the normal state is insulating. In the white-, green-, and rainbow-colored regions, the A_{1u} pairing induces nodal, fully gapped (FG), and gapless but easily gappable (EG) superconductivity, respectively. The yellow- and red-colored regions in the right figure represent the trivial superconductor ($\mathcal{Z} = 0$) and the second-order TSC ($\mathcal{Z} = 1$), respectively. (b) The topological phase diagrams for the E_u IR with C_{3z} eigenvalue $\alpha = \omega$. The yellow, blue, orange, cyan, magenta, and purple regions represent the phases with $\mathcal{C} = 0$, $\mathcal{C} = 1$, $\mathcal{C} = 2$, $\mathcal{C} = 3$, $\mathcal{C} = 4$, and $\mathcal{C} = 5$ modulo 6, respectively. For $\alpha = \omega^2$, the sign of $\mathcal{C}$ becomes reversed. (c) The evolution of the phase diagram from the nonmagnetic case to the ferromagnetic case (left) and the noncollinear AFM case in (b) (right). To consider a situation where both P and C_{3z} are conserved, we assume out-of-plane ordered ferromagnetism in the left. Then, the ferromagnetic phase diagram can be simply obtained by superposing spin-up and spin-down phase diagrams, while the AFM phase diagram shows a more complex structure.

In the case of gapped superconducting states, its topological properties can be described by using the symmetry indicators [55–58]. When the pairing interaction is weak enough, the symmetry representations of the occupied states of $\mathcal{H}_{\rm BdG}(\boldsymbol{k})$ at high-symmetry momenta remain unchanged after the superconducting phase transition. Thus, regardless of the detailed form of the pairing interaction, one can draw the phase diagrams using the symmetry indicator information extracted from the normal state and pairing symmetry as discussed in detail in Supplemental Material [25]. This approximation is valid if the pairing interaction is smaller than the bandwidth of electron bands at the Fermi level. Since the band structure of kagome lattice noncollinear antiferromagnet has nearly flat bands lying between $E = 2$ and $2 + m$ (i.e., m is the bandwidth for these bands), we expect the weak-coupling approximation would be valid for $\mu < 2$ or large m values. The distribution of the invariant $\mathcal{Z}$ related to the second-order topology for the A_{1u} IR and that of the Chern number for the E_u IR, obtained by using the symmetry indicators,

are shown in Figs. 3(a) and 3(b), respectively. The corresponding Wilson loop and edge spectra are described in Supplemental Material [25].

We note that the spin texture induced by noncollinear AFM ordering also affects the topological nature of the gapped superconducting states. To illustrate this, we compare the superconducting phase diagram of the kagome ferromagnet and that of the noncollinear antiferromagnet considering the E_u IR, as shown in Fig. 3(c). In the case of the ferromagnet without winding spin texture, the superconducting phase diagram can be understood by using the relevant phase diagram for spinless band structure with $m = 0$. Since the ferromagnetism only induces a rigid shift of spin-up and spin-down bands, the superconducting phase diagram of the ferromagnet is merely a simple superposition of two $m = 0$ phase diagrams for spin-up and spin-down electrons, respectively. On the other hand, in the case of a noncollinear antiferromagnet, as the winding spin texture accompanies normal state band degeneracies associated with the singular points of the $\boldsymbol{R}$ field, which are absent in the ferromagnet, the corresponding superconducting phase diagram exhibits distinct topological characteristics.

Discussion.—In this Letter, we have studied the effect of real space magnetic texture on the FS and its superconductivity. Especially, it is shown that spin-momentum locking on the FS can be generated purely by the real space magnetism even in the absence of SOC. This magnetism-induced FSST, together with the d vector, provides an intuitive understanding of the symmetry-protected nodes on high-symmetry lines in noncollinear AFM superconductors. To support our theory further, we have performed additional first-principles calculation for a kagome coplanar antiferromagnet Mn_3Sn illustrating the FSST, and mean-field analysis about superconducting instability arising from phenomenological density-density interaction, as described in detail in Supplemental Material [25].

We emphasize that the scope of our theory is not restricted to the kagome lattice in 2D. It can be applied to a general two- or three-dimensional lattice with an arbitrary number of sublattices. Indeed, consistent with our prediction on the requirements to have winding spin texture, a recent spin-resolved angle-resolved photoemission spectroscopy measurement reported that $MnTe_2$ [59], a noncoplanar antiferromagnet that has four atoms in the magnetic unit cell with linearly dependent local spin moments, shows winding spin texture. Finally, considering our prediction of various odd-parity spin-triplet superconducting states with intriguing nodal structures and topological properties, we expect that the kagome AFM is poised to become a crucial arena for Majorana engineering in magnetic superconductors.

S. H. L., Y. Q., and B.-J. Y. were supported by Samsung Science and Technology Foundation under Project No. SSTF-BA2002-06, and National Research Foundation of Korea (NRF) grants funded by the government of Korea (MSIT) (Grants No. 2021R1A2C4002773 and No. NRF-2021R1A5A1032996).

*bjyang@snu.ac.kr

[1] M. Sigrist and K. Ueda, Rev. Mod. Phys. **63**, 239 (1991).
[2] W. Kohn and J. Luttinger, Phys. Rev. Lett. **15**, 524 (1965).
[3] P. W. Anderson and W. F. Brinkman, Phys. Rev. Lett. **30**, 1108 (1973).
[4] D. Vollhardt and P. Wolfle, *The Superfluid Phases of Helium 3* (Courier Corporation, North Chelmsford, MA, 2013).
[5] A. C. Potter and P. A. Lee, Phys. Rev. B **83**, 184520 (2011).
[6] M. Smidman, M. Salamon, H. Yuan, and D. Agterberg, Rep. Prog. Phys. **80**, 036501 (2017).
[7] Y. Li and Z.-A. Xu, Adv. Quantum Technol. **2**, 1800112 (2019).
[8] M. Desjardins, L. Contamin, M. Delbecq, M. Dartiailh, L. Bruhat, T. Cubaynes, J. Viennot, F. Mallet, S. Rohart, A. Thiaville, A. Cottet, and T. Kontos, Nat. Mater. **18**, 1060 (2019).
[9] S. Yoshizawa, T. Kobayashi, Y. Nakata, K. Yaji, K. Yokota, F. Komori, S. Shin, K. Sakamoto, and T. Uchihashi, Nat. Commun. **12**, 1462 (2021).
[10] X. Zhang, J. Liu, and F. Liu, Nano Lett. **22**, 9000 (2022).
[11] G. Chang, B. J. Wieder, F. Schindler, D. S. Sanchez, I. Belopolski, S.-M. Huang, B. Singh, D. Wu, T.-R. Chang, T. Neupert *et al.*, Nat. Mater. **17**, 978 (2018).
[12] S. H. Lee, H. C. Choi, and B.-J. Yang, Phys. Rev. Lett. **126**, 067001 (2021).
[13] L. Šmejkal, R. González-Hernández, T. Jungwirth, and J. Sinova, Sci. Adv. **6**, eaaz8809 (2020).
[14] L. Šmejkal, J. Sinova, and T. Jungwirth, Phys. Rev. X **12**, 031042 (2022).
[15] L. Šmejkal, J. Sinova, and T. Jungwirth, Phys. Rev. X **12**, 040501 (2022).
[16] M. T. Mercaldo, C. Noce, A. D. Caviglia, M. Cuoco, and C. Ortix, npj Quantum Mater. **8**, 12 (2023).
[17] M. Naka, S. Hayami, H. Kusunose, Y. Yanagi, Y. Motome, and H. Seo, Nat. Commun. **10**, 4305 (2019).
[18] M. Naka, S. Hayami, H. Kusunose, Y. Yanagi, Y. Motome, and H. Seo, Phys. Rev. B **102**, 075112 (2020).
[19] M. Naka, Y. Motome, and H. Seo, Phys. Rev. B **103**, 125114 (2021).
[20] M. Naka, Y. Motome, and H. Seo, Phys. Rev. B **106**, 195149 (2022).
[21] S. Sumita, M. Naka, and H. Seo, Phys. Rev. Res. **5**, 043171 (2023).
[22] Y. Noda, K. Ohno, and S. Nakamura, Phys. Chem. Chem. Phys. **18**, 13294 (2016).
[23] T. Okugawa, K. Ohno, Y. Noda, and S. Nakamura, J. Phys. Condens. Matter **30**, 075502 (2018).
[24] M. Kawano and C. Hotta, Phys. Rev. B **100**, 174402 (2019).
[25] See Supplemental Material at http://link.aps.org/supplemental/10.1103/PhysRevLett.132.196602 for more detailed derivation of the Fermi surface spin texture equation, the effective Hamiltonian projected to sublattices,

superconducting state belonging to E_u irreducible representation, topological invariants for superconducting states, first-principles calculations of Mn_3Sn, and mean-field analysis of the superconducting states in kagome antiferromagnet, which includes Refs. [26–45].

[26] C. Bradley and A. Cracknell, *The Mathematical Theory of Symmetry in Solids* (Oxford University Press, New York, 2010).
[27] X.-L. Qi, Y.-S. Wu, and S.-C. Zhang, Phys. Rev. B **74**, 045125 (2006).
[28] L. Fu and E. Berg, Phys. Rev. Lett. **105**, 097001 (2010).
[29] M. Sato, Phys. Rev. B **81**, 220504(R) (2010).
[30] T. Fukui, K. Shiozaki, T. Fujiwara, and S. Fujimoto, J. Phys. Soc. Jpn. **81**, 114602 (2012).
[31] C.-K. Chiu, J. C. Y. Teo, A. P. Schnyder, and S. Ryu, Rev. Mod. Phys. **88**, 035005 (2016).
[32] E. Khalaf, Phys. Rev. B **97**, 205136 (2018).
[33] J. Ahn and B.-J. Yang, Phys. Rev. Res. **2**, 012060(R) (2020).
[34] S. A. A. Ghorashi, T. L. Hughes, and J. Cano, arXiv: 2306.09413.
[35] K. Kuroda, T. Tomita, M.-T. Suzuki, C. Bareille, A. Nugroho, P. Goswami, M. Ochi, M. Ikhlas, M. Nakayama, S. Akebi *et al.*, Nat. Mater. **16**, 1090 (2017).
[36] S. Tomiyoshi, J. Phys. Soc. Jpn. **51**, 803 (1982).
[37] P. Brown, V. Nunez, F. Tasset, J. Forsyth, and P. Radhakrishna, J. Phys. Condens. Matter **2**, 9409 (1990).
[38] S. V. Gallego, J. M. Perez-Mato, L. Elcoro, E. S. Tasci, R. M. Hanson, K. Momma, M. I. Aroyo, and G. Madariaga, J. Appl. Crystallogr. **49**, 1750 (2016).
[39] K. Momma and F. Izumi, J. Appl. Crystallogr. **44**, 1272 (2011).
[40] G. Kresse and J. Furthmüller, Comput. Mater. Sci. **6**, 15 (1996).
[41] G. Kresse and J. Furthmüller, Phys. Rev. B **54**, 11169 (1996).
[42] G. Kresse and D. Joubert, Phys. Rev. B **59**, 1758 (1999).
[43] J. P. Perdew, K. Burke, and M. Ernzerhof, Phys. Rev. Lett. **80**, 891 (1998).
[44] U. Herath, P. Tavadze, X. He, E. Bousquet, S. Singh, F. Muñoz, and A. H. Romero, Comput. Phys. Commun. **251**, 107080 (2020).
[45] D. Sénéchal, A.-M. Tremblay, and C. Bourbonnais, *Theoretical Methods for Strongly Correlated Electrons* (Springer Science & Business Media, New York, 2006).
[46] Z. Xiao, J. Zhao, Y. Li, R. Shindou, and Z.-D. Song, arXiv:2307.10364.
[47] J. Ahn, D. Kim, Y. Kim, and B.-J. Yang, Phys. Rev. Lett. **121**, 106403 (2018).
[48] J. Ahn, S. Park, and B.-J. Yang, Phys. Rev. X **9**, 021013 (2019).
[49] D. E. Almeida, R. M. Fernandes, and E. Miranda, Phys. Rev. B **96**, 014514 (2017).
[50] B. Powell, J. F. Annett, and B. Györffy, J. Phys. A **36**, 9289 (2003).
[51] S. Sachdev, Phys. Rev. B **45**, 12377 (1992).
[52] S. Hayami, Y. Yanagi, and H. Kusunose, Phys. Rev. B **102**, 144441 (2020).
[53] S. Hayami, Y. Yanagi, and H. Kusunose, Phys. Rev. B **101**, 220403(R) (2020).
[54] P. A. McClarty and J. G. Rau, Phys. Rev. Lett. **132**, 176702 (2024).
[55] A. Skurativska, T. Neupert, and M. H. Fischer, Phys. Rev. Res. **2**, 013064 (2020).
[56] S. Ono, H. C. Po, and H. Watanabe, Sci. Adv. **6**, eaaz8367 (2020).
[57] S. Ono, H. C. Po, and K. Shiozaki, Phys. Rev. Res. **3**, 023086 (2021).
[58] L. Elcoro, B. J. Wieder, Z. Song, Y. Xu, B. Bradlyn, and B. A. Bernevig, Nat. Commun. **12**, 5965 (2021).
[59] Y.-P. Zhu, X. Chen, X.-R. Liu, Y. Liu, P. Liu, H. Zha, G. Qu, C. Hong, J. Li, Z. Jiang *et al.*, Nature (London) **626**, 523 (2024).